

Natural magmatic granite as matrix for immobilizing simulated An^{4+} waste

Lingshuang Li

Southwest University of Science and Technology

Xiaoyan Shu

Southwest University of Science and Technology

Hexi Tang

Southwest University of Science and Technology

Shunzhang Chen

Sichuan University

Wenxiao Huang

Ministry of Land and Resources

Guilin Wei

Southwest University of Science and Technology

Dadong Shao

Nanjing University of Science and Technology

Yi Xie

University of Science and Technology of China

Xirui Lu (✉ luxiruimvp116@163.com)

Southwest University of Science and Technology <https://orcid.org/0000-0003-4751-8408>

Research Article

Keywords: Granite immobilization, Simulated An^{4+} waste, Solubility, Glass-ceramics

Posted Date: April 23rd, 2020

DOI: <https://doi.org/10.21203/rs.3.rs-23879/v1>

License: © ⓘ This work is licensed under a Creative Commons Attribution 4.0 International License.

[Read Full License](#)

Abstract

In nature, many rocks contain radionuclides, and returning radioactive waste to nature is an environmentally friendly way. In this work, a natural magmatic granite rock has been studied as a host matrix for simulated An^{4+} waste disposal. The blank granite, in the form of powder, was firstly treated by muffle furnace heating in the temperature range of 800 °C to 1400 °C. It was found that the lowest crystallinity of the samples was obtained at 1300 °C. Moreover, 8 wt.% of simulated tetravalent actinides (CeO_2) could be successfully immobilized in the natural granite at 1300 °C for 60 min. Raman results show the structure disordering in samples tends to increase with the increased amount of CeO_2 . SEM-EDS observation shows that the distribution of Ce was relatively uniform in the matrix. Moreover, the hardness of solidified body is comparable to traditional glasses and it decreases with the increase of CeO_2 content.

1. Introduction

With the development of nuclear power and national defense industry, the amount of radioactive waste increased. Actinides in high-level waste (HLW) presents high specific activity, long half-life and high toxicity. If not properly handled, it will seriously endanger the living environment of human beings. At present, deep geological disposal has been widely recognized [1–3]. To ensure long-term safety during disposal, one of the keys is to immobilize waste in a stable matrix to prevent nuclides migration or leakage. As the first barrier between high-level radioactive waste and biosphere, the safety and stability of the main matrix in a long time are particularly important.

Hatch *et al.* [4] first proposed minerals to fix radionuclides so that nuclear waste should return to nature like natural radionuclides, and to maintain long-term safety and stability. Now, Synroc is known as the second generation of matrix for immobilizing high-level radioactive waste. It has the characteristics of strong inclusiveness, high water resistance, low nuclides leaching rate, considerable thermal stability and good radiation resistance [5–8]. Up to now, high-alunite phases, titanium-based phases, silicon-based ore phases and its composite phase are recognized as candidate solidified bodies for long-lived radioactive waste [9–13]. With the aim of solidifying radioactive waste to nature, most of these researches concerned Synroc. Until 2007, B. I. Omel'yanenko *et al.* [14] proved the feasibility of using natural minerals to return radioactive waste to nature by studying both natural minerals and Synroc. However, a large amount of work, from material selection to performance evaluation, is still required.

This work chose natural magmatic granite as host matrix to simulated An^{4+} waste, since the rock integrity of granite is highly recognized by geologists all over the world. Granite is mainly composed of quartz, plagioclase, K-feldspar, biotite and hornblende etc. [15]. And it has the characteristics of small porosity, low water content, poor water permeability, large elongation, and good stability, which contributes to prevent or delay the migration of radionuclides [16]. In addition, granite belongs to a glass-ceramic matrix, which has the advantages of both glass and ceramics. The basic principle shows in

Fig. 1. In this experiment, blank granite powder was sintered to find a suitable sintering temperature, and then Ce^{4+} was doped as simulated tetravalent actinide oxides to study the solidification behavior of natural magmatic granite [17–19]. The phase, micro-morphology and mechanical properties of the immobilization were characterized.

2. Experimental

2.1 Fabrication

The rock sample was collected at Tong'an in northeast of Guangxi. Zhu *et al.* [20] determined the geological age of the Tong'an quartz monzonite as 160 ± 4 Ma. The collected rock was mechanically broken up. Then the broken rock was fully washed with water in an ultrasonic cleaner and alcohol in turn to remove surface sludge. The clean rock was dried at $90\text{ }^\circ\text{C}$ for 12 h in a drier and then crushed in a high speed universal crusher (TASITE FW100, Tianjin) to produce powder through 200 mesh. The crushed sample was subjected to further refining by grinding with adding alcohol. The X-ray Fluorescence (XRF) result of the pure granite powder was listed in Table 1, it presented characteristic of higher alumina element content.

Table 1
Contents of the pristine granite

Compound	SiO ₂	Al ₂ O ₃	CaO	Fe ₂ O ₃	MgO	Na ₂ O	K ₂ O	TiO ₂	P ₂ O ₅
Conc.(%)	59.28	17.03	6.74	6.37	3.74	3.55	1.83	0.76	0.31
Compound	Cr ₂ O ₃	MnO	SrO	BaO	ZrO ₂	ZnO	Rb ₂ O	Y ₂ O ₃	Total
Conc.(%)	0.13	0.11	0.07	0.04	0.02	0.01	0.01	0.00	100.03

The powder was dried again and compressed into tablets ($\varphi = 13$ mm) under 16 MPa. The tablets were sintered in a muffle furnace at $800\text{ }^\circ\text{C}$, $900\text{ }^\circ\text{C}$, $1000\text{ }^\circ\text{C}$, $1100\text{ }^\circ\text{C}$, $1200\text{ }^\circ\text{C}$, $1300\text{ }^\circ\text{C}$ and $1400\text{ }^\circ\text{C}$ respectively for 60 minutes. Sintered temperature was controlled by heating program, which was set to a heating rate of $5\text{ }^\circ\text{C}/\text{min}$. After being kept at the highest temperature for 60 min, the sintered samples were naturally cooled down to room temperature. The whole sintered process was conducted in air atmosphere.

The rock and CeO₂ powder (Tianjin Kermel Co. Ltd., purity $\geq 99.99\%$) were weighed according to the content of CeO₂ was 5 wt.%, 10 wt.%, 15 wt.% and 20 wt.% respectively. The mixed powder was further ground and compressed into tablets under a pressure of 14 MPa. Then the samples were sintered in a muffle furnace at $1300\text{ }^\circ\text{C}$ for 60 minutes and naturally cooled down to room temperature. The whole experiment process is as shown in Fig. 2. The morphology did not change significantly until the sintering temperature reached $1100\text{ }^\circ\text{C}$. Melting was observed beyond $1200\text{ }^\circ\text{C}$.

2.2 Characterization

The composition of the rock powder was analyzed by X-ray fluorescence (XRF Axios, Netherlands $\theta/2\theta$, 2.4 kW). The results are showed in Table 1. To identify the phase structure of the samples, X-ray diffractometer (XRD D/MAX-1400, Rigaku Corporation) with Cu K α radiation was applied with scanning range of 10 ° to 80 ° at scanning speed of 2 °/min. To observe the micro-morphology of the samples, scanning electron microscopy coupled with energy dispersive X-ray spectroscopy (SEM-EDS, TM4000, Hitachi, Japan) was used. In addition, the samples were also characterized by Raman spectroscopy (InVia laser Raman spectrometer manufactured by Renishaw Company, UK) to study molecular structure. Specimens were carefully polished to get a flat indentation face for the Vickers hardness test (TMVS-1S, China). 4.9 N was applied for indentation for three time on each sample to calculate the average value.

3. Results And Discussion

3.1 Phase analysis through XRD

3.1.1 Effect of temperature on the structure of pure granite

Fig. 3 (a) shows XRD patterns of virgin and sintered pure granite samples obtained below 1200 °C. There are mainly quartz, feldspar, and a little amount of chromite in the virgin granite. As the sintering temperature ranged from 800 °C to 1200 °C, all the diffraction peaks existed with varied intensity. The intensity of quartz and feldspar gradually weakened with enhanced temperatures, while the intensity of chromite became gradually strong. This is due to the decomposition of feldspar as the temperature rose and the quartz gradually vitrified^[21]. Fig. 3 (b) presents the pure granite sintered at 1300 °C and 1400 °C. Feldspar and quartz almost disappeared after heat treated beyond 1300 °C, and chromite became the main phase. In addition, diffuse scattering peak ranging from 15 ° to 33 ° emerged, reflecting the amorphous phase of glass structure. Co-existence of amorphous and chromite phase indicated a glass-ceramic matrix of sintered samples. Moreover, a more disordered glass network structure under increased temperatures was disclosed from the weakening and broadening of diffuse scattering peak^[22].

Fig. 4 presents the crystallinity of the pure granite sintered at different temperatures. The sample sintered at 800 °C showed the highest crystallinity of about 80 %. As the temperature increased, the crystallinity of the sample decreases gradually. At 1300 °C, the sample exhibited the minimum crystallinity of about 52 %. Then, the crystallinity turned to increase with sintering temperature by improving the proportion of chromite. According to Fig. 3, the crystallinity reduced due to the phase transformation of granite from crystal to an amorphous state. At 1300 °C, there is a obvious characteristic peak of glassy amorphization, and the crystallinity reached the lowest level. Subsequently, the intensity of diffuse scattering peak reduced, the crystallinity of the sample increased.

3.1.2 Effect of the CeO₂ content

According to the XRD results obtained from blank granite, magmatic rocks was selected as host material to immobilize simulated tetravalent actinides at 1300 °C for 60 minutes. Figure 5 shows the XRD patterns of samples doped with 0 ~ 20 wt.% of CeO₂. When the content is 5 wt.%, no CeO₂ related peaks can be detected. As the doping amount reached 10 wt.%, some peaks related to CeO₂ appeared on the XRD pattern, indicating that granite cannot immobilize CeO₂ over this content. It reflects that the ultimate solubility of the simulated tetravalent actinide oxides in granite was between 5 ~ 10 wt.%. In order to further study the ultimate solubility, CeO₂ was doped into pure granite powder with the content of 6 wt.%, 7 wt.%, 8 wt.%, and 9 wt.%, and sintered at 1300 °C for 60 min. Figure 6 presents the XRD results of the samples with the doping amounts of CeO₂ from 5 wt.% to 10 wt.%. As the doping content of CeO₂ below 8 wt.%, only the diffuse scattering peak and the diffraction peaks of chromite were detected, while the diffraction peaks related to CeO₂ are absent. When the amount of CeO₂ reach 9 wt.%, the diffraction peaks of CeO₂ were observed. It indicates that the ultimate solubility of simulated tetravalent actinide oxides in granite is about 8 wt.%. In the solidified body, amorphous phase exists together with chromite crystals, which suggests a glass-ceramic structure.

3.2 Raman analysis

Fig. 7 shows the Raman spectra (300~900 cm⁻¹) of fabricated samples holding different contents of CeO₂. All the samples with different doping amount of CeO₂ present a high intensity peak at around 680 cm⁻¹, which belongs to Si-O-Si bending vibration [23]. There is a characteristic band appears in the range of 500-600 cm⁻¹, which corresponded to Al-O-Al linkages [24,25]. The weak peak near 462 cm⁻¹ belongs to Ce-O vibration, according to literatures [26,27]. Fig. 7 shows the intensity of the peak at 680 cm⁻¹ gradually increases as the doping amounts below 7 wt.%. However, the peak turns to becomes weak and wide as the doping amount beyond 8 wt.%. In addition, the Raman vibration spectra peak at 680 cm⁻¹ shifted towards higher frequencies with increased CeO₂ content, which can be explained by the substitution of Si atom by increased Al in the symmetric stretching mode of Si-O-Si (Q⁴) [23]. The schematic process in glass is presented in Fig. 8. It shows the structural disordering tends to increase with increased CeO₂ and the main Raman spectroscopy inclines to be homogeneous [28,29].

3.3 Microtopography analysis

Fig. 9 presents the SEM micrograph and Energy-dispersive spectroscopy (EDS) of samples with various doping content of CeO₂ (6 wt.%, 7 wt.%, 8 wt.%, 9 wt.% and 10 wt.%) to investigate the doping effects of CeO₂ effects on the microstructure evolution. It can be seen from Fig. 9 (a₁), (b₁) and (c₁) that the surface of the samples was smooth and bright, which is essentially consistent with the macro-profile and the XRD results that these samples are mainly glass. However, obvious crystals precipitate on the sample surface with over enhanced CeO₂ content, just as shown in Fig. 9 (d₁) and (e₁).

Energy-dispersive spectroscopy (EDS) was also used to evaluate compositional distribution of the samples holding different doping content of CeO₂ [30, 31], and the element mapping of Si, O, Ce and Al are

illustrated in Fig. 9. It can be seen that all the elements in the solidified bodies were relatively uniform without enrichment, which indicates that the simulated nuclides Ce is uniformly solidified into granite. Combined Fig. 9 (d₁) to (d₅) with XRD, Raman and SEM results, it can be concluded that the precipitate crystals are CeO₂.

3.4 Vickers hardness analysis

Fig. 10 gives the Vickers hardness of samples, whose content of CeO₂ is from 0 *wt.*% to 20 *wt.*%. It can be found that the hardness shows a gradual reduce with enhanced CeO₂. The lowest hardness (4.91 GPa) is got in the sample with the highest doping content and the highest hardness value (6.88 GPa) is obtained in the blank granite sample. Among different content, it can be concluded by fixing the Ce content that the hardness mainly shows an reduce trend. Especially when the doping amount from 5 *wt.*% to 10 *wt.*%, the trend of decrease is quickly. When the content of CeO₂ reached the limit solubility (8 *wt.*%), the hardness value is 5.79 GPa, and it is reduced by 15.75% compared to the blank granite. In addition, the hardness of the samples is a little higher than traditional Na₂O-TiO₂-SiO₂ glasses (4.5-5.5 GPa) [32], while it is lower than some alkali and alkaline earth aluminum silicate glasses (6.8~7.8 GPa) [33].

4. Conclusions

Natural magmatic granite was selected to investigate the feasibility of immobilizing simulated tetravalent actinides CeO₂. Based on a series of bank granite were sintered at the temperature from 800 °C to 1400 °C for 60 minutes. And a series of solidification doped with CeO₂ were sintered by conventional furnace heating at 1300 °C for 60 minutes. The maximum solubility of CeO₂ is 8 *wt.*% and Ce may be involved in the glass network structure, SEM-EDS results show that Ce is uniform in the matrix and there is no regional enrichment. Raman results indicate that structural disorder increases with CeO₂ content increase. Moreover, the solidified samples show their Vickers hardness values between traditional Na₂O-TiO₂-SiO₂ glasses and alkali and alkaline earth aluminum silicate glasses. This experiment provides a potential possibility to return radioactive nuclear waste to nature.

Declarations

Acknowledgements

The authors appreciate the financial supports from the National Natural Science Foundation of China (No. 21976146) and the Research Fund Program of Guangdong Key Laboratory of Radioactive and Rare Resource Utilization (No.2019-LRRRU02).

References

1. Briggs S, Mckelvie J, Sleep B, et al. Multi-dimensional transport modelling of corrosive agents through a bentonite buffer in a Canadian deep geological repository[J]. *Science of The Total Environment*, 2017, 599–600:348–354.
2. Zhang CL, Conil N, Armand G. Thermal Effects on Clay Rocks for Deep Disposal of High-Level Radioactive Waste[J]. *J Rock Mech Geotech Eng*. 2016;9(3):81–96.
3. Malkovsky VI, Yudintsev SV, Sharaputa MK, et al. Influence of buoyancy forces on movement of liquid radioactive waste from deep injection disposal site in the Tomsk region, Russian Federation: analytical estimate and numerical modeling[J]. *Environmental Earth Sciences*, 2019, 78(6).
4. Hatch LP. Ultimate disposal of radioactive wastes[J]. *American Scientist*, 1953: 410–421.
5. Amoroso J, Marra JC, Tang M. Melt processed multiphase ceramic waste forms for nuclear waste immobilization [J]. *J Nucl Mater*. 2014;454(1–3):12–21.
6. Weber WJ, Navrotsky A, Stefanovsky S. Materials science of high-level nuclear waste immobilization [J]. *Mater Res Bull*. 2009;34(1):46–531.
7. Weber WJ, Ewing RC, Catlow CRA, et al. Radiation effects in crystalline ceramics for the immobilization of high-level nuclear waste and plutonium [J]. *J Mater Res*. 1998;13(6):1434–84.
8. Sabathier C, Chaumont J, Rouzière S, Traverseb A. Characterisation of Ti and Sr atomic environments in SrTiO₃ before and after ion beam irradiation by X-ray absorption spectroscopy [J]. *Mater*. 1998;13(6):1434–84.
9. Mandal BP, Grag N, Sharma SM, et al. Solubility of ThO₂ in Gd₂Zr₂O₇ pyrochlore: XRD, SEM and Raman spectroscopic studies[J]. *J Nucl Mater*. 2009;392(1):95–9.
10. Nästren C, Jardin R, Somer J, et al. Actinide incorporation in a zirconia based pyrochlore (Nd_{1.8}An_{0.2})Zr₂O_{7+x} (An = Th, U, Np, Pu, Am) [J]. *Solid State Chem*. 2009;182:1–7.
11. Donald IW, et al. The immobilization of high level radioactive wastes using ceramics and glasses[J]. *Journal of Materials Science*, 1997, 32, 5851–5887.
12. Dawson J, Hill P, Kinny P. Mineral chemistry of a zircon-bearing, composite, veined and metasomatised upper-mantle peridotite xenolith from kimberlite[J]. *Contrib Miner Petrol*. 2001;140(6):720–33.
13. Cheary RW, Coelho AA. A site occupancy analysis of zirconolite CaZr_xTi_{3-x}O₇[J]. *Physics chemistry of minerals*. 1997;24(6):447–54.
14. Omel'yanenko BI, Livshits TS, Yudintsev SV, et al. Natural and artificial minerals as matrices for immobilization of actinides[J]. *Geol Ore Deposits*. 2007;49(3):173–93.
15. Baik MH, Cho WJ, Hahn PS.. A Parametric Study on the Sorption of U(VI) onto Granite[J]. 2004.
16. Tsai S-C, Wang T-H, Li M-H, Wei Y-Y. Shi-Ping Teng, Cesium adsorption and distribution onto crushed granite under different physicochemical conditions[J]. *J Hazard Mater*. 2009;161(2–3):854–61.
17. Lu X, Cui C, Song G, et al. Capability of zircon as radioactive waste forms for immobilizing tetravalent actinides[J]. *China Environmental Science*. 2011;6:012.

18. Jiali X, Kuibao Z, Zongsheng H, et al. Rapid disposal of simulated Ce-bearing radioactive soil waste using self-propagating synthesized zirconolite-rich waste matrice[J]. *Ceram Int*. 2018;44(12):14534–40.
19. Chen S, Liu X, Shu X, et al. Rapid synthesis and chemical durability of Gd₂Zr₂-xCe_xO₇ via SPS for nuclear waste forms[J]. *Ceramics International*,2018,44(16): 20306–20310.
20. Zhu JC, Xie CF, Zhang PH, Yang C, Gu CY. Niumiao and Tong'an intrusive bodies of NE Guangxi: Petrology, zircon SHRIMP U-Pb geochronology and geochemistry[J]. *Acta Petrologica Sinica*. 2005;21(3):665–76.
21. Lu X, Chen S, Shu X, et al. Immobilisation of nuclear waste by microwave sintering with a natural magmatic rock[J]. *Philos Mag Lett*. 2018;98(4):155–60.
22. Xiaoyan Shu Y, Li W, Huang, et al. Solubility of Nd³⁺ and Ce⁴⁺ in co-doped simulated radioactive contaminated soil after microwave vitrification[J]. *Ceramics International*,2020,46(5): 6767–6773.
23. Sarfraz Ahmad MM, Mahmoud. Hans Jürgen Seifert, Crystallization of two rare-earth aluminosilicate glass-ceramics using conventional and microwave heat-treatments[J]. *J Alloy Compd*. 2019;797:45–57.
24. Kucharczyk S, Sitarz M, Zajac M, et al. The effect of CaO/SiO₂ molar ratio of CaO-Al₂O₃-SiO₂ glasses on their structure and reactivity in alkali activated system[J]. *Spectrochimica Acta Part A Molecular Biomolecular Spectroscopy*. 2018;194:163–71.
25. Mcmillan P, Piriou B, Navrotsky A. A Raman spectroscopic study of glasses along the joins silica-calcium aluminate, silica-sodium aluminate, and silica-potassium aluminate[J]. *Geochim Cosmochim Acta*. 1982;46(11):2021–37.
26. Brogan MS, Dines TJ, Cairns JA. Raman spectroscopic study of the Pt-CeO₂ interaction in the Pt/Al₂O₃-CeO₂ catalyst, *J. Chem. Soc. Faraday Trans. 90* (1994). 1461–1466.
27. Jiali X, Kuibao Z, Zongsheng H, et al. Rapid disposal of simulated Ce-bearing radioactive soil waste using self-propagating synthesized zirconolite-rich waste matrice[J]. *Ceram Int*. 2018;44(12):14534–40.
28. Chen S, Shu X, Wang L, et al. Effects of alpha irradiation on Nd₂Zr₂O₇ matrix for nuclear waste forms[J]. *Journal of the Australian Ceramic Society*, 2017.
29. Lu X, Shu X, Wang L, et al. Heavy-ion irradiation effects on Gd₂Zr₂O₇ ceramics bearing complex nuclear waste[J]. *J Alloy Compd*. 2019;771:973–9.
30. Xie Y, Fan L, Shu X, et al. Chemical stability of Ce-doped zircon ceramics: Influence of pH, temperature and their coupling effects[J]. *J Rare Earths*. 2017;35(2):164–71.
31. Siwińska N, Ąak A, Słowikowska M, et al. Morphology and elemental analysis of free range and stabled Polish Konik horses hair using Energy-dispersive X-ray spectroscopy (EDS)[J]. *Polish Journal of Veterinary Sciences*. 2018;21(1):65–72.
32. Scannell G, Laille D, Célarié F, et al. Interaction between deformation and crack initiation under Vickers indentation in Na₂O-TiO₂-SiO₂ glasses[J]. *Frontiers in Materials*. 2017;4:6.

33. Tiegel M, Hosseinabadi R, Kuhn S, et al. Young's modulus, Vickers hardness and indentation fracture toughness of aluminosilicate glasses[J]. Ceram Int. 2015;41(6):7267–75.

Figures

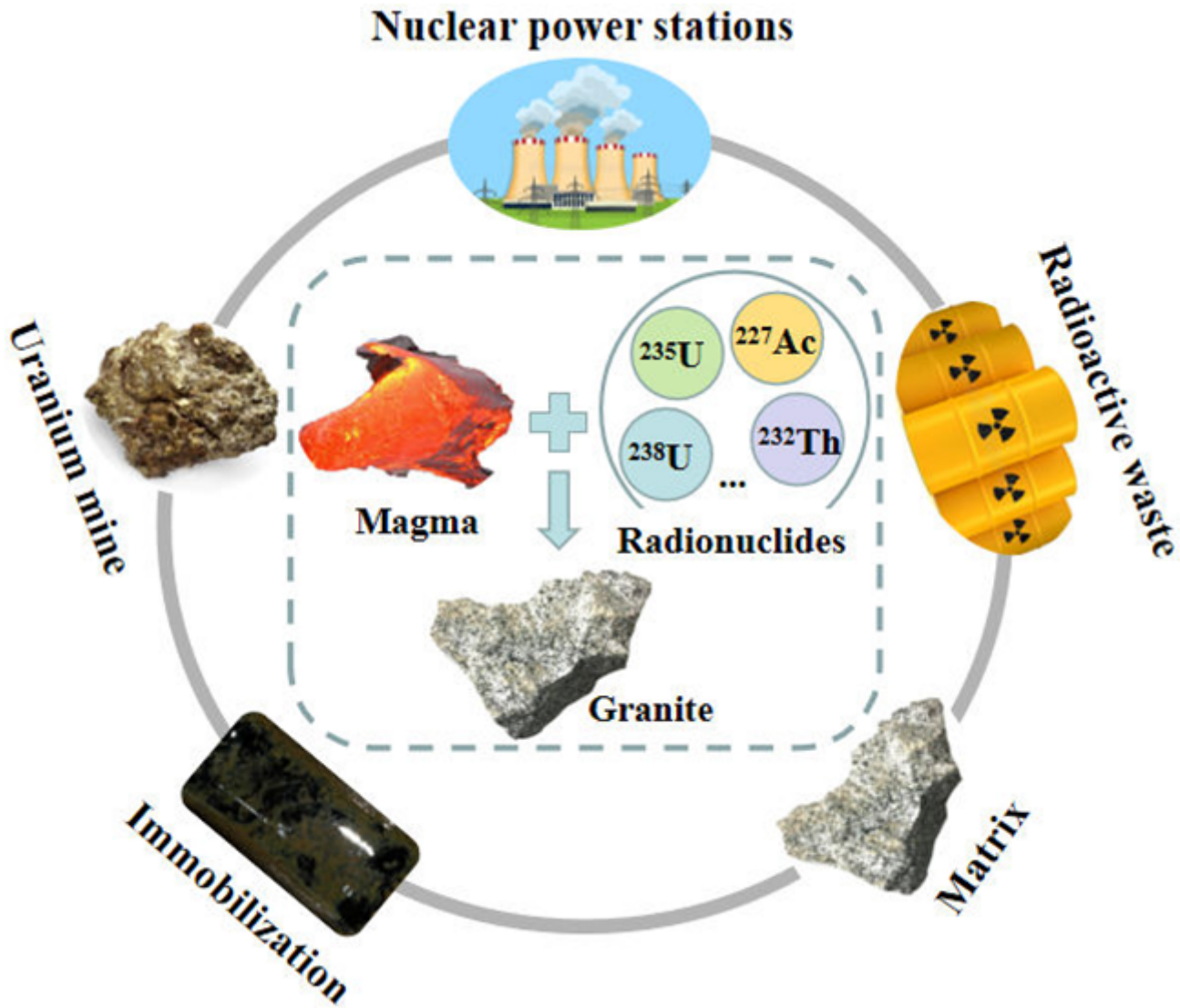


Figure 1

Schematic of granite immobilize radioactive waste

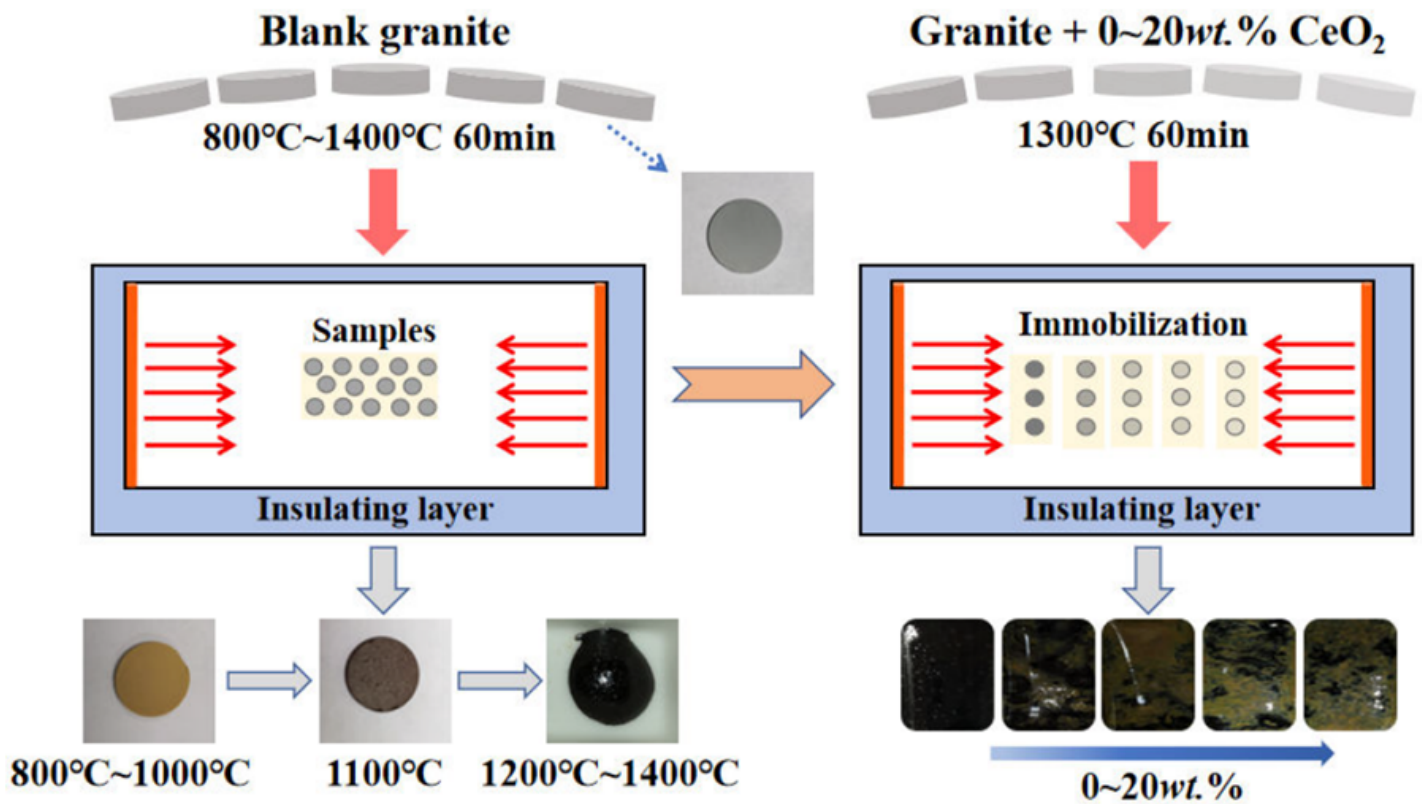


Figure 2

Schematic of experimental process

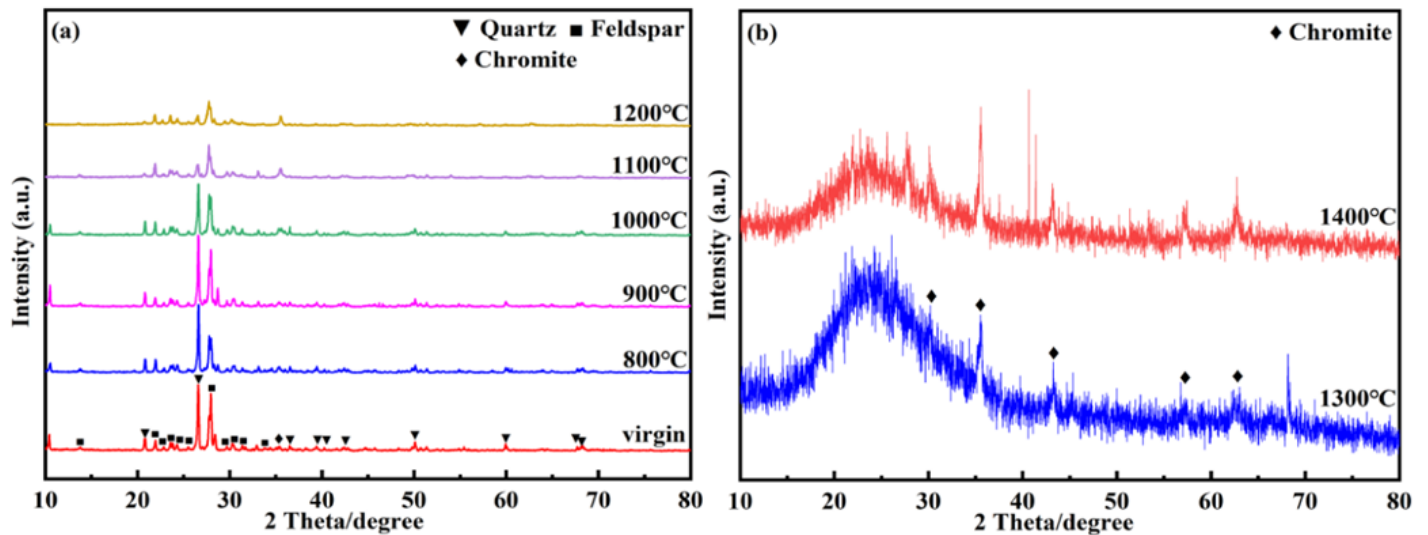


Figure 3

XRD patterns of pure granite (a) virgin and sintered samples from 800 °C to 1200 °C (b) samples obtained at 1300 °C and 1400 °C

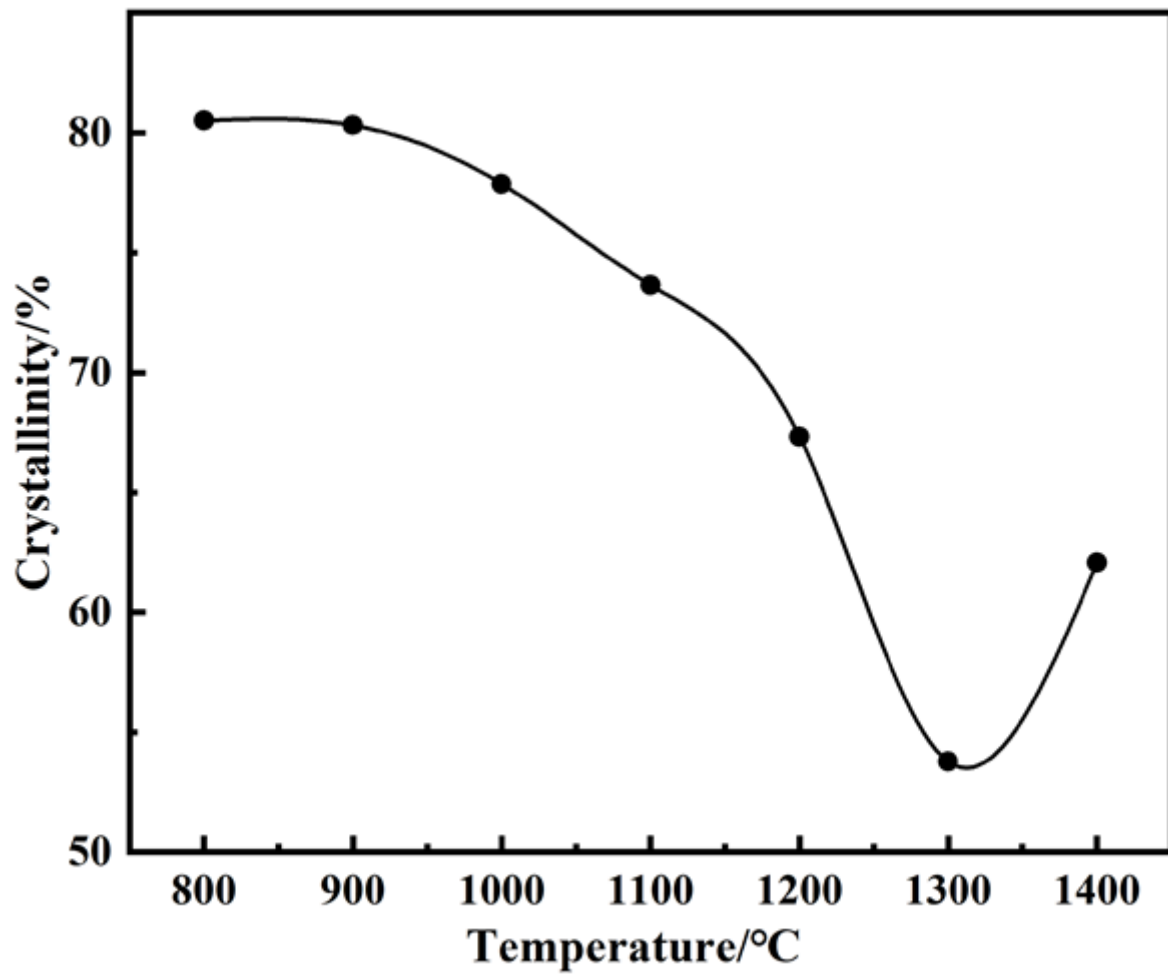


Figure 4

Crystallinity of pure granite samples sintered at different temperatures

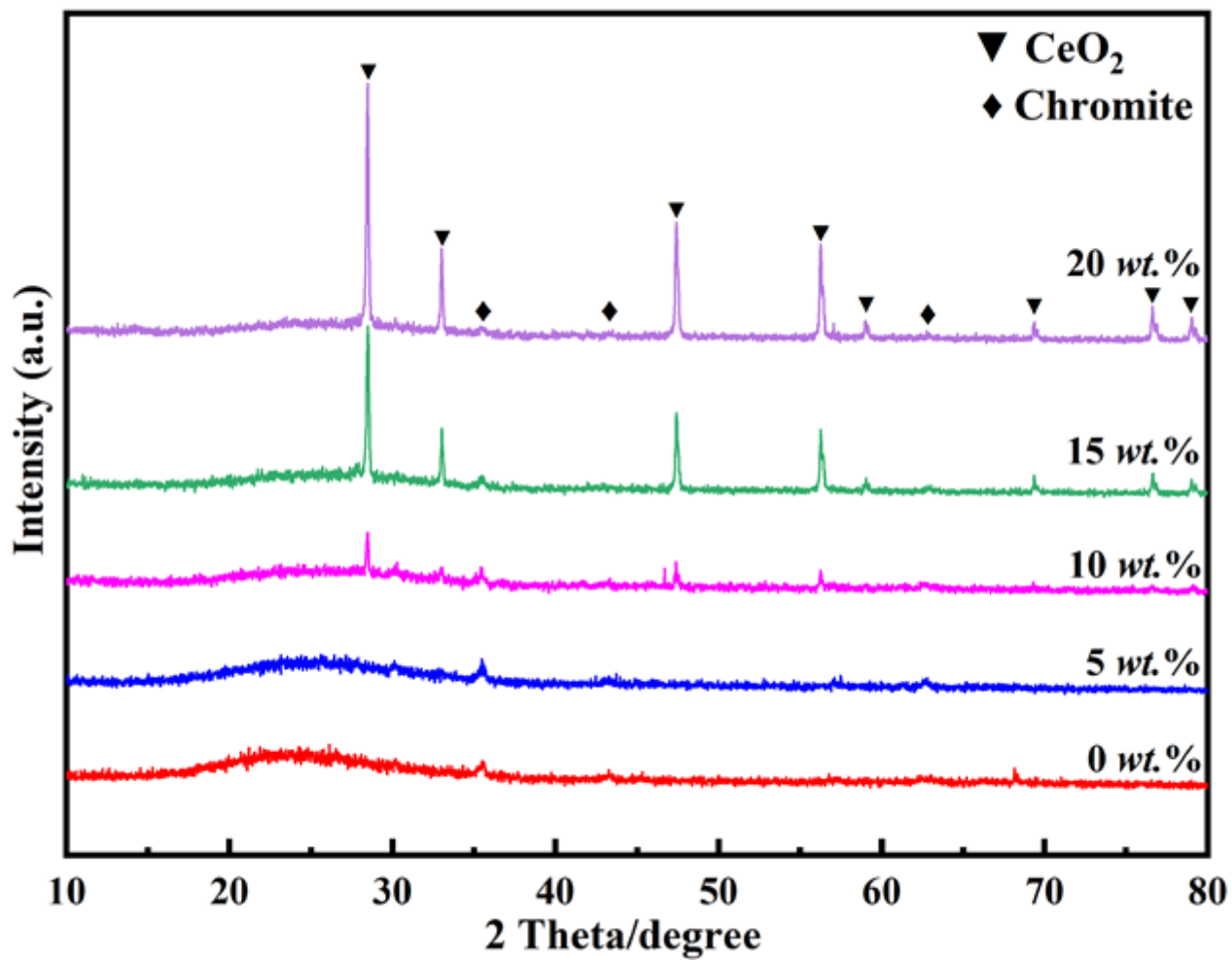


Figure 5

XRD patterns of the samples with the doping amounts of CeO₂ from 0 wt.% to 20 wt.%

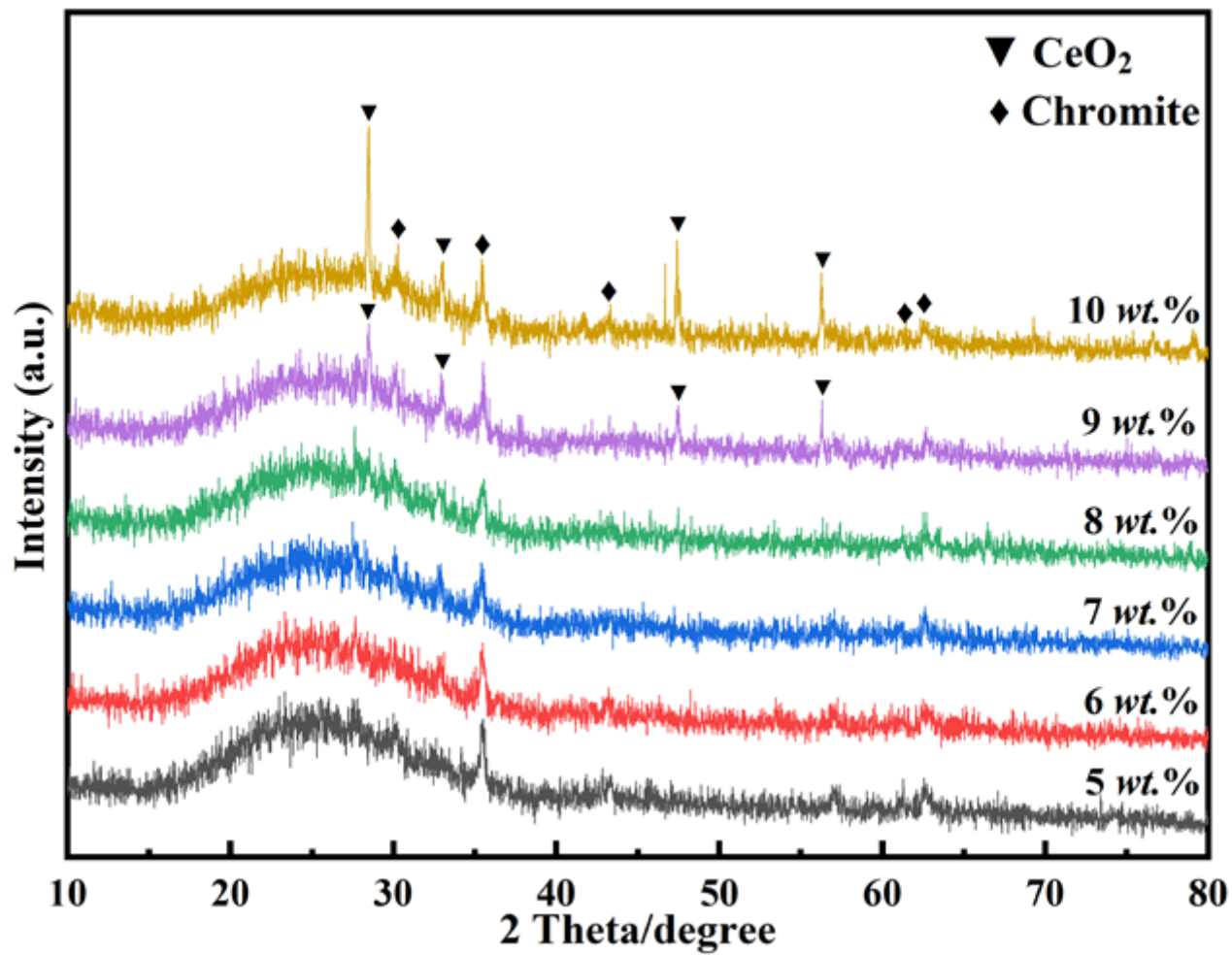


Figure 6

XRD patterns of the samples with the doping content of CeO₂ from 5 wt.% to 10 wt.% (a) 6 wt.% (b) 7 wt.% (c) 8 wt.%

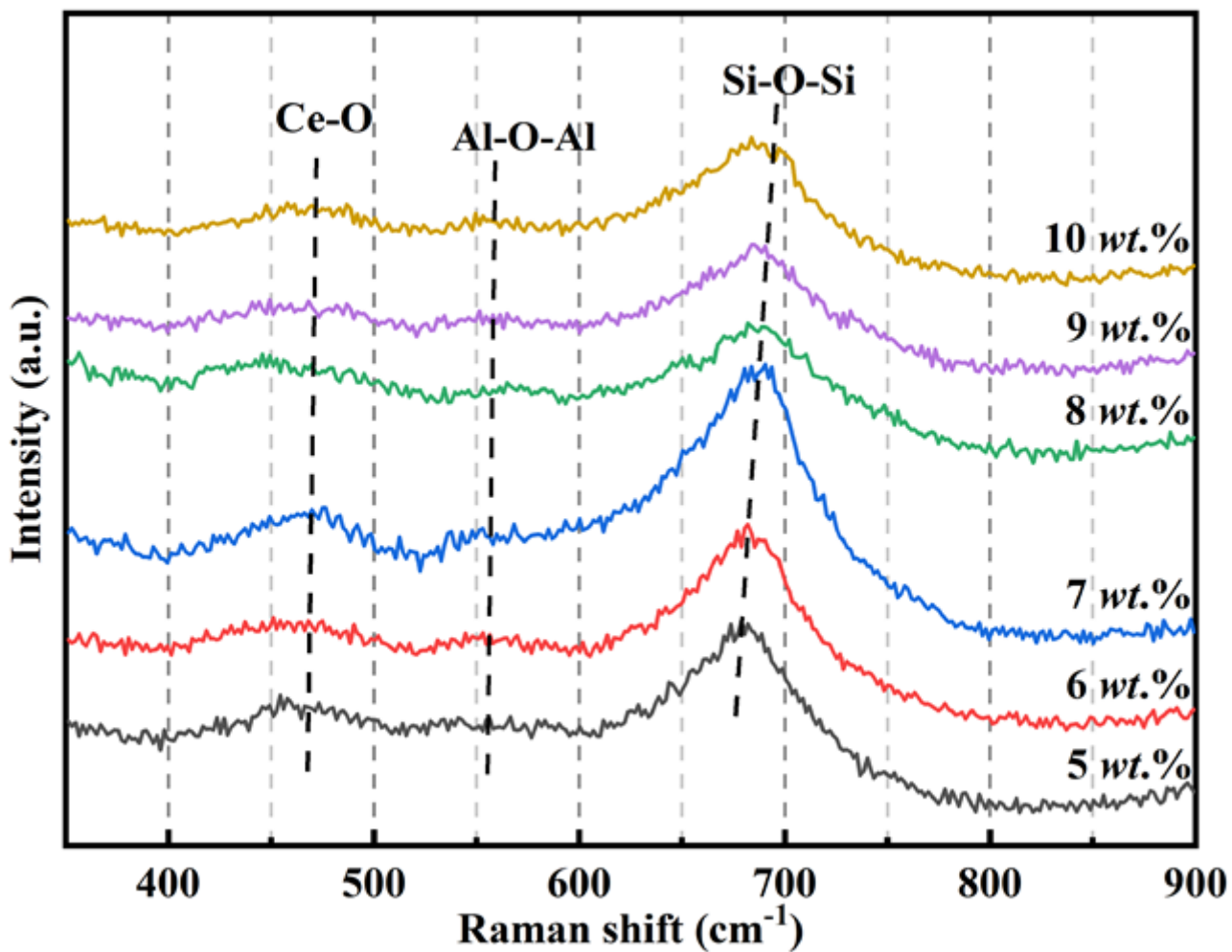


Figure 7

The Raman spectra of the samples with the doping amounts of CeO₂ from 5 wt.% to 10 wt.%

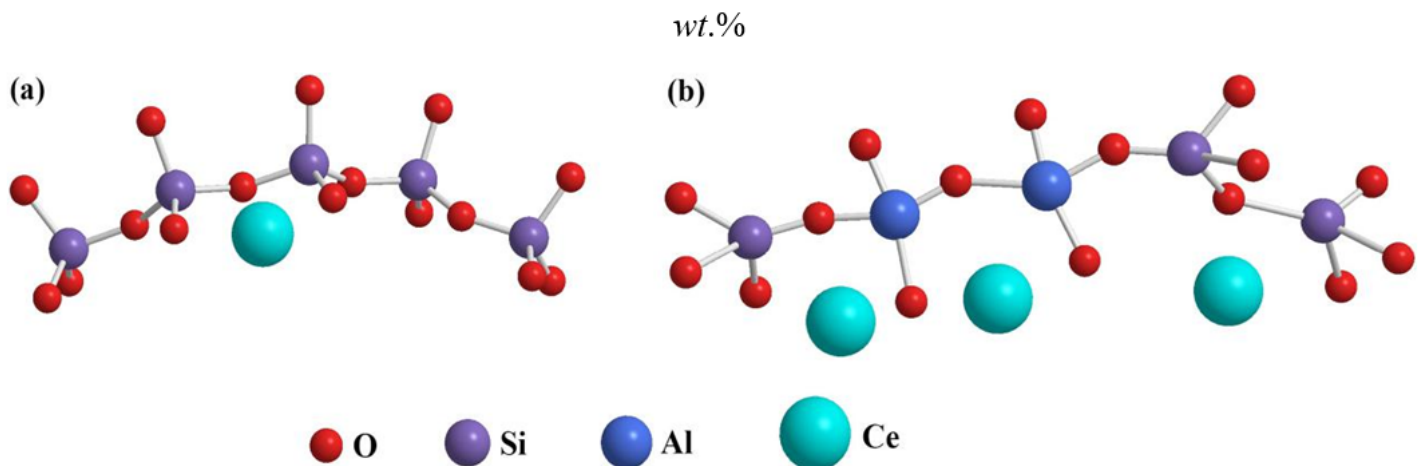


Figure 8

Schematic of immobilizing CeO₂ in glass phase of granite matrix at (a) low doping (b) high doping

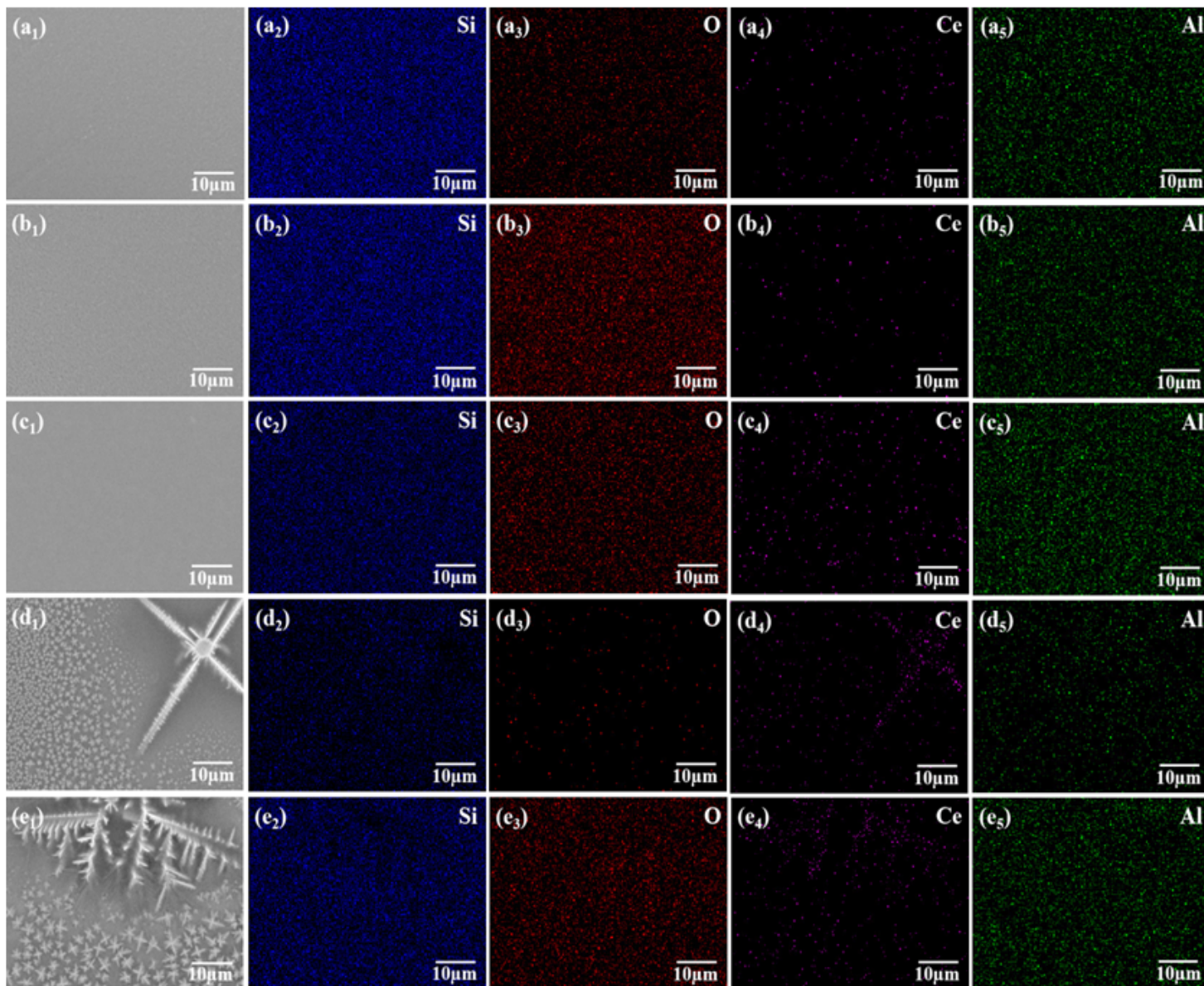


Figure 9

SEM-EDS of samples and immobilized different amount of CeO₂ (a) 6 wt.% (b) 7 wt.% (c) 8 wt.% (d) 9 wt.% (e) 10 wt.%

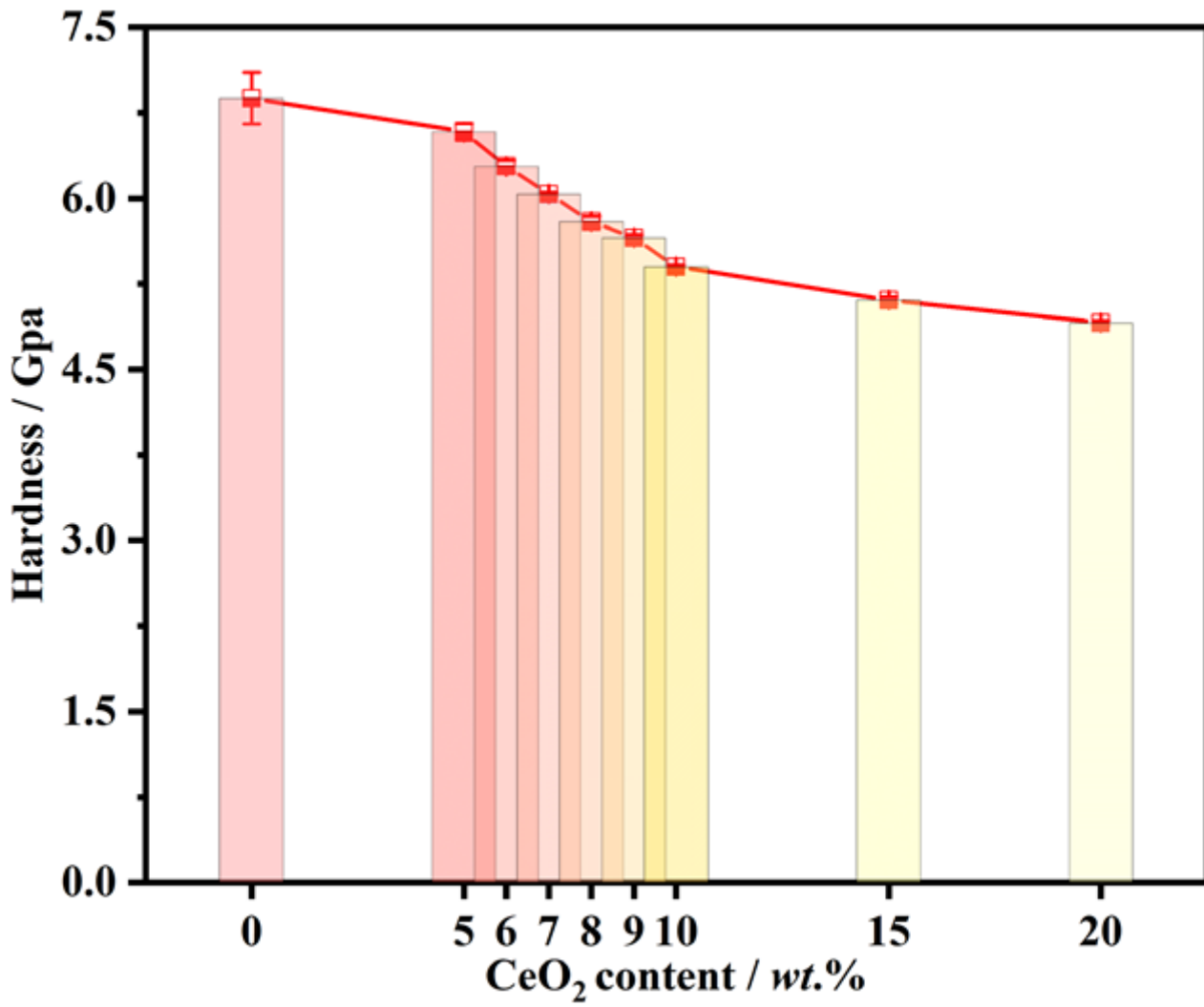


Figure 10

Vickers hardness of sample with holding CeO₂ from 0 wt.% to 20 wt.%